PHYSICAL REVIEW B **98**, 014110 (2018)

Topological interface modes in local resonant acoustic systems

Degang Zhao,[1,2] Meng Xiao,[2] C. W. Ling,[3] C. T. Chan,[2] and Kin Hung Fung[3,*]
[1]*Department of Physics, Huazhong University of Science and Technology, Wuhan, 430074, China*
[2]*Department of Physics, Hong Kong University of Science and Technology, Clear Water Bay, Hong Kong, China*
[3]*Department of Applied Physics, The Hong Kong Polytechnic University, Hong Kong, China*

(Received 12 December 2017; revised manuscript received 11 July 2018; published 27 July 2018)

Topological phononic crystals are artificial periodic structures that can support nontrivial acoustic topological bands, and their topological properties are linked to the existence of topological edge modes. Most previous studies have been focused on the topological edge modes in Bragg gaps, which are induced by lattice scattering. While local resonant gaps would be of great use in subwavelength control of acoustic waves, whether it is possible to achieve topological interface states in local resonant gaps is a question. In this paper, we study the topological properties of subwavelength bands in a local resonant acoustic system and elaborate the band-structure evolution using a spring-mass model. Our acoustic structure can produce three band gaps in the subwavelength region: one originates from the local resonance of unit cell and the other two stem from band folding. It is found that the topological interface states can only exist in the band-folding-induced band gaps, but never appear in the local resonant band gap. In addition, the numerical simulation in a practical system perfectly agrees with the theoretical results. Our study provides an effective approach of producing robust acoustic topological interface states in the subwavelength region.

DOI: 10.1103/PhysRevB.98.014110

I. INTRODUCTION

Over the past decades, topological properties have attracted extensive research interests in electronic materials [1,2], mechanical metamaterials [3–5], photonic systems [6–8], and phononic systems [9–17]. Topological invariants, such as the Chern number [1–17] and Zak phase [18–20], can be used to characterize the topological properties of bands. The most fascinating phenomenon in these topological systems is the bulk-edge correspondence associated with topologically protected edge modes, which are one-way propagation modes along the surface or interface and are immune to lattice defects. For one-dimensional (1D) periodic systems, the Su-Schrieffer-Heeger (SSH) model was proposed to explain the existence of topological edge modes in polyenes chain [21], and these states have recently been observed experimentally [22]. The SSH model has served as a paradigmatic example of a 1D topological system and has been quickly extended to optical systems [23–26] and mechanical systems [4]. Recently, Zhang *et al.* proposed an acoustic SSH model consisting of a 1D array of acoustic resonators, and revealed topological interface states in the lowest Bragg-like gap [27,28]. Most of the previous works focused on the topological properties in Bragg band gaps due to Bragg scattering. In acoustic systems, another essential mechanism to open band gaps is the local resonance, which stems from the resonance of individual scattering unit [29]. The questions arise whether topological edge states can exist in local resonant gaps. What are the topological invariants of the local resonant bands? To answer these questions, in this paper we build a spring-mass model to describe the bands of a 1D SSH chain hybridized with extra local resonances and systematically demonstrate the evolution of band structure and topological properties of all subwavelength bands. In addition, we verify the theoretical results by performing a numerical simulation of transmission spectra and field distribution in a practical 1D SSH lattice.

II. SPRING-MASS MODEL

Before considering topological acoustic systems with local resonances, we first begin with a simple infinitely long monatomic chain consisting of mass-in-mass local resonant unit cells, which is schematically presented in Fig. 1(a). Each unit cell can be modeled as a spherical shell of mass M connected to a mass m by two massless springs with equal spring constants G. All of the neighboring units are connected by massless springs with spring constants K with a nearest center-to-center distance of a. The dispersion relation of such a mass-in-mass monatomic chain is given by

$$M_{\mathrm{eff}}(\omega)\omega^2 = 4K\sin^2\frac{qL}{2}, \tag{1}$$

where $M_{\mathrm{eff}}(\omega) = M + \frac{m\omega_0^2}{\omega_0^2-\omega^2}$ denotes the effective mass of the local resonant unit cell, $\omega_0 = \sqrt{2G/m}$ is the local resonance frequency, q is the Bloch wave number, and $L = a$ is the lattice constant. The dispersion relation in Eq. (1) is plotted in Fig. 1(d) for $M = 2.0$, $m = 0.5$, $K = 1.25$, and $\omega_0 = 1.0$. A typical local resonant band gap appears when the frequency ω approaches ω_0. At such local resonance frequency, $M_{\mathrm{eff}} \to \infty$, meaning that the oscillator is effectively too heavy and does not have any response on the external applied force. Consequently, q does not have a real solution in Eq. (1) and a local resonant band gap is opened at $\omega \approx \omega_0$.

---

[*] khfung@polyu.edu.hk

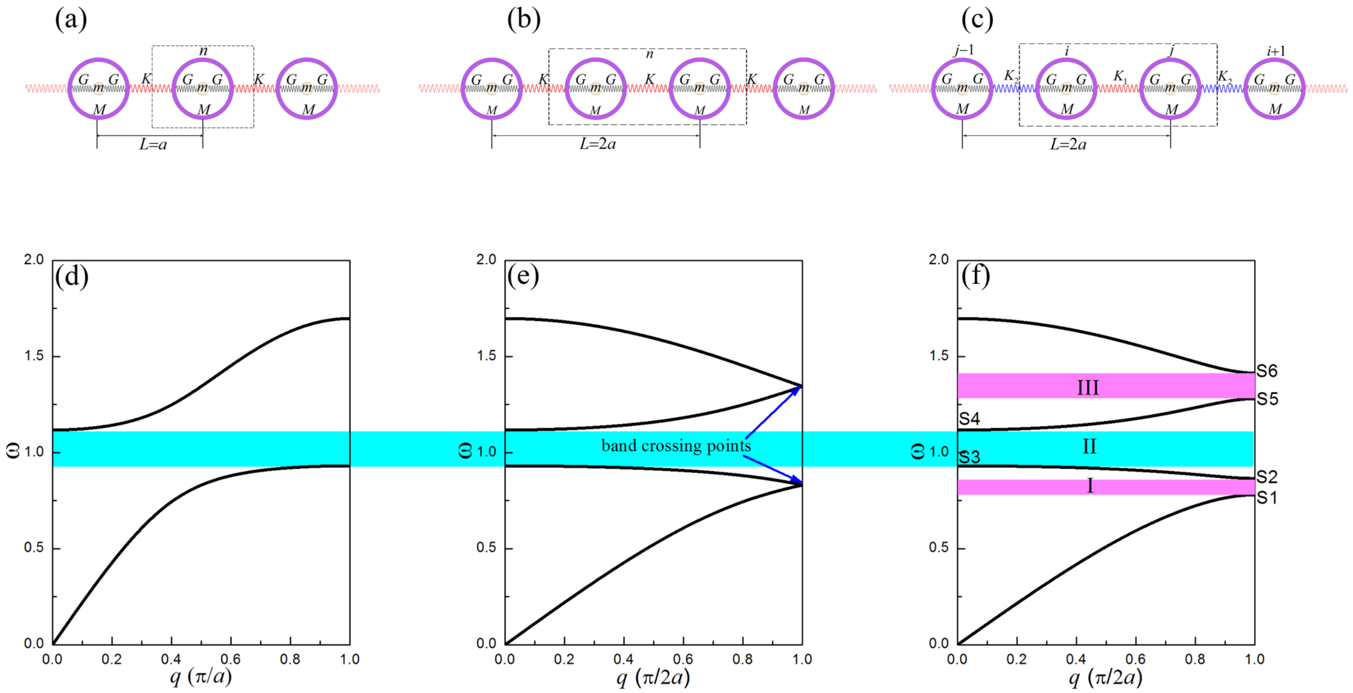

FIG. 1. Schematics of the spring-mass model of a 1D array of local resonant unit cells in (a) monatomic chain, (b) a chain identical to that in (a) except that the new unit cell consists of two unit cells in (a), and (c) diatomic chain with $K_1 \neq K_2$. The dashed frames mark the unit cells for these three distinct chains. L denotes the lattice constant. (d), (e), and (f) are the band structures for the systems depicted in (a), (b), and (c), respectively. The cyan and magenta strips represent the local resonant gaps and band-folding-induced gaps, respectively. The three gaps in (f) are indicated by Roman numerals I, II, and III. S1–S6 in (f) denotes the band edges of all gaps.

Next in Fig. 1(b), the unit-cell size is doubled compared to that in Fig. 1(a), i.e., $L = 2a$, and the other parameters remain unchanged. The Brillouin zone for the new choice of unit cell in Fig. 1(b) is thus reduced to a half of that for the unit cell in Fig. 1(a). The band structure of this diatomic chain in Fig. 1(b) can be obtained by folding the band structure along the midline of the Brillouin zone in Fig. 1(d), as shown in Fig. 1(e). Further, based on the structure in Fig. 1(b), we make the left and right springs of each oscillator have different spring constants K_1 and K_2, as depicted in Fig. 1(c), forming a so-called SSH chain [21]. Instead of writing a 4×4 matrix problem, the motion equations can be transformed into an eigenvalue problem involving a 2×2 matrix:

$$\begin{pmatrix} 0 & K_1 + K_2 e^{-iqL} \\ K_1 + K_2 e^{iqL} & 0 \end{pmatrix} \begin{pmatrix} u_i \\ u_j \end{pmatrix} = \lambda \begin{pmatrix} u_i \\ u_j \end{pmatrix}, \quad (2)$$

where u_i and u_j are the displacements of M in one unit cell. The frequency dependence appears only in the eigenvalues $\lambda(\omega) = [K_1 + K_2 - M_{\text{eff}}(\omega)\omega^2]$ and the eigenvectors. The eigenvalue $\lambda(\omega)$ is a monotonic function of ω except at the jump at ω_0. Therefore, the eigenvalue problem in Eq. (2) forms a two-to-one mapping to that of the SSH model without resonance. For example, the zero-energy eigenvalue in the SSH model without resonance is mapped to the two positive-frequency solutions ω_n satisfying the quartic (fourth-order power) equation $K_1 + K_2 - M_{\text{eff}}(\omega_n)\omega_n{}^2 = 0$.

By searching for the nontrivial solutions of Eq. (2), the following dispersion relation for a SSH chain can be obtained:

$$\cos qL = 1 - \frac{M_{\text{eff}}\omega^2(2K_1 + 2K_2 - M_{\text{eff}}\omega^2)}{2K_1K_2}. \quad (3)$$

The detailed derivation of Eqs. (1), (2), and (3) can be found in Appendix A, the corresponding band structure calculated by Eq. (3) is plotted in Fig. 1(f) with $K_1 = 1.0$, $K_2 = 1.5$, and all of the other parameters are identical to that in Fig. 1(e). As is well known, the patterns of local resonant band gap and Bragg band gap are very different. Generally speaking, for a local resonant band gap, its lower band terminates at the boundary of the Brillouin zone and its upper band emerges at the center of the Brillouin zone [see Fig. 1(d)]. However for a Bragg band gap, the termination of the lower band and emergence of the upper band will both occur at the boundary or center of the Brillouin zone. By simply observing the band-structure patterns, all three band gaps in Fig. 1(f) seem to be Bragg band gaps. However, the band-structure evolution [from Figs. 1(d) to 1(f)] suggests that band gap II essentially originates from the local resonance of the individual scattering unit. It is evident that this band gap survives in all three structures. When $K_1 = K_2 = K$, the first and second bands, third and fourth bands will meet at the folding points [see Fig. 1(e)], which can be regarded as the topological phase-transition points [19,27,28]. When $K_1 \neq K_2$, these two band-crossing points open to become gaps I and III (see Appendix B), which can be regarded as the band-folding-induced gaps.

We now investigate the topology of all of the bulk bands in Fig. 1(f) by evaluating the Zak phase [18]. Combining Eqs. (A3) and (A9) in Appendix A, the eigenvector of a SSH chain can be obtained:

$$(u_i, v_i, u_j, v_j)^T = \left(\pm e^{i\phi(q)}, \pm \frac{\omega_0^2}{\omega_0^2 - \omega^2} e^{i\phi(q)}, 1, \frac{\omega_0^2}{\omega_0^2 - \omega^2} \right)^T, \quad (4)$$

TABLE I. Sign of $\varsigma^{(n)}$ for SSH chains with $K_1 < K_2$ and $K_1 > K_2$.

	$K_1 < K_2$	$K_1 > K_2$
$\mathrm{sgn}[\varsigma^{(\mathrm{I})}]$	$+$	$-$
$\mathrm{sgn}[\varsigma^{(\mathrm{II})}]$	$+$	$+$
$\mathrm{sgn}[\varsigma^{(\mathrm{III})}]$	$+$	$-$

TABLE II. Signs of eigenstates at band edges.

		$K_1 < K_2$	$K_1 > K_2$
Band gap I	S1	$(-,-,+,+)^T$	$(+,+,+,+)^T$
	S2	$(+,+,+,+)^T$	$(-,-,+,+)^T$
Band gap II	S3	$(-,-,+,+)^T$	$(-,-,+,+)^T$
	S4	$(+,-,+,-)^T$	$(+,-,+,-)^T$
Band gap III	S5	$(-,+,+,-)^T$	$(+,-,+,-)^T$
	S6	$(+,-,+,-)^T$	$(-,+,+,-)^T$

where $\phi(q) = \arg(K_1 + K_2 e^{-iqL})$. The superscript T denotes the transpose operation. The ± signs in Eq. (4) are determined by the signs of the eigenvalues of Eq. (2) (see Appendix C). The Zak phase [19,23] can thus be obtained from the eigenvectors as

$$\theta = i\int_{-\pi/L}^{\pi/L} dq\langle\Psi|\partial_q|\Psi\rangle = -\frac{\phi(\frac{\pi}{L}) - \phi(-\frac{\pi}{L})}{2} = \begin{cases}\pi, & K_1 < K_2\\ 0, & K_1 > K_2\end{cases}, \tag{5}$$

where $|\Psi\rangle$ is the eigenvector normalized by the kinetic energy. The definition of $|\Psi\rangle$ and the detailed Zak-phase calculations can be found in Appendix D. Equation (5) indicates that all four bulk bands in Fig. 1(f) have the same quantized Zak phase, either 0 or π. The lattice in Fig. 1(c) has only one definite band structure, but a different unit-cell choice ($K_1 < K_2$ or $K_1 > K_2$) would lead to different topological properties of bands. If two semi-infinite SSH chains with $K_1 < K_2$ and $K_1 > K_2$ are combined to form a whole block, the existence of topological edge states in the nth band gaps can be determined by the bulk-edge correspondence. It is only necessary to know the sign of $\varsigma^{(n)}$, which is defined as [19]

$$\mathrm{sgn}[\varsigma^{(n)}] = (-1)^n \exp\left(i\sum_{m=0}^{n-1}\theta^{(m)}\right). \tag{6}$$

For the nth band gaps, if the $K_1 < K_2$ and $K_1 > K_2$ chains have different $\mathrm{sgn}[\varsigma^{(n)}]$, topological edge states will definitely exist in the band gaps. Conversely, if they have the same $\mathrm{sgn}[\varsigma^{(n)}]$, topological edge states cannot exist. Table I lists $\mathrm{sgn}[\varsigma^{(n)}]$ as calculated for all three band gaps. From Table I, it can be seen that for two distinct SSH chains, $\mathrm{sgn}[\varsigma^{(n)}]$ differs in band gaps I and III, but is the same in band gap II. Thus, topological edge states can only exist in band gaps I and III, but not in band gap II. In other words the original local resonant band gap will not support any topological edge states, which are produced simultaneously in two band-folding-induced band gaps.

Another criterion to determine the existence of topological edge states is the switching of the field distribution of eigenstates at the two band-edge points [marked by S1,S2, …, S6 in Fig. 1(f)] of each isolated band gap for two different SSH chains, which is known as "band inversion" transition [2,19]. Since the two different SSH chains have identical band structures, it is only necessary to calculate the sign of the eigenvector components u_i, v_i, u_j, v_j, which are listed in Table II. The detailed calculations can be found in Appendix C. For the band-folding-induced gaps, viz., band gap I and III, the states of the lower and upper band edges indeed switch upon changing $K_1 < K_2$ to $K_1 > K_2$. However, the states do not undergo any changes in band gap II, viz., the local resonant band gap. Thus, the topological edge states will definitely only exist in band gaps I and III, but not in band gap II. This result is consistent with Zak-phase analysis.

To verify the analytical derivations, we construct a supercell spring-mass system to calculate the dispersion relation of interface states. The supercell is composed of a SSH chain with $K_1 < K_2$ on the left connected to another SSH chain with $K_1 > K_2$ on the right. The band structure of the connected chain system is shown in Fig. 2(a). It distinctly exhibits two extra flat bands, i.e., topological interface states appearing only in the first and third band gaps, which agree with analytical predictions. To demonstrate the evolution of the topological interface states, we keep the left chain unchanged, and investigate the dependence of the band structure on the ratio of the spring constants K_1/K_2 of the right chain. The results are presented in Fig. 2(b). When $K_1/K_2 < 1$, all of the bulk bands of the left and right chains, although they have different frequency regions, have the same topological properties. Based on the bulk-edge correspondence, the topological interface states certainly will not appear in common band gaps. However, when $K_1/K_2 > 1$, the topology of all of the bulk bands of the right chain is converted, and topological interface states obviously emerge in the first and third band gaps. Thus these interface states are topologically protected and robust at the same frequency.

III. SUBWAVELENGTH TOPOLOGICAL INTERFACE STATES IN A PRACTICAL SYSTEM

In this section we describe a practical structure that yields topological interface states in the subwavelength region. The system is a 1D array of "core-shell" cylinders, as depicted in Fig. 3(a). Each cylinder consists of an epoxy core (mass density $\rho = 1180\ \mathrm{kg/m^3}$, longitudinal wave velocity $c_l = 2540\ \mathrm{m/s}$, and transverse wave velocity $c_t = 1160\ \mathrm{m/s}$) coated by soft rubber (mass density $\rho = 1300\ \mathrm{kg/m^3}$, longitudinal wave velocity $c_l = 50\ \mathrm{m/s}$, and transverse wave velocity $c_t = 20\ \mathrm{m/s}$), and they are immersed in water background (mass density $\rho = 1000\ \mathrm{kg/m^3}$, longitudinal wave velocity $c = 1490\ \mathrm{m/s}$). We adjust the separation of the two cylinders in one unit cell to mimic the different spring constants K_1 and K_2 in the spring-mass model. The separation of the left lattice is $d_L(<L/2)$ and that of the right lattice is $d_R(>L/2)$, and for simplicity we set $d_L + d_R = L$ to guarantee that the left and right lattices would have identical band structures. We perform the numerical simulation by using the commercial finite-element software COMSOL MULTIPHYSICS.

The lowest four bulk bands of the left or right lattice individually are plotted in Fig. 3(b). All three band gaps are in the subwavelength region with normalized frequencies lower

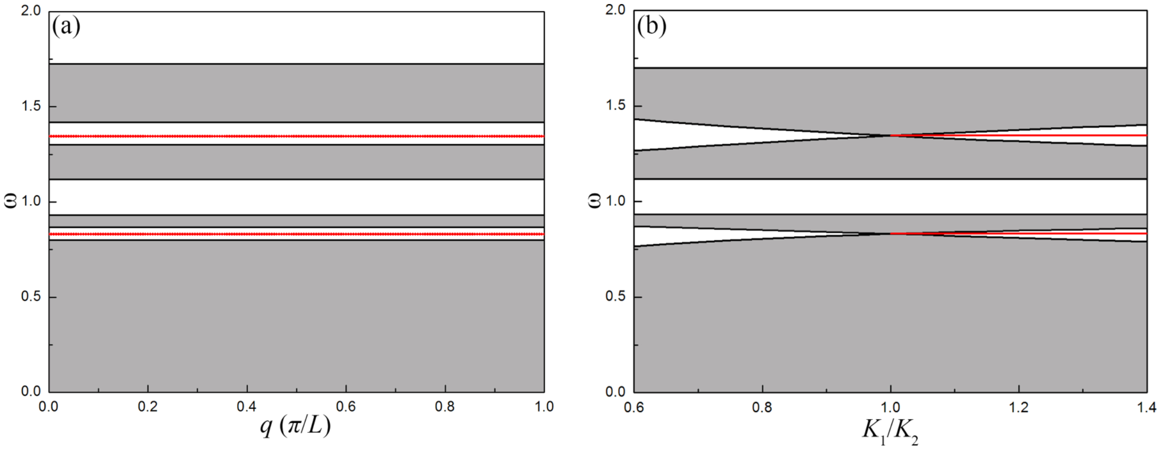

FIG. 2. (a) Topological interface states (red lines) of a supercell system composed of a SSH chain with $K_1 < K_2$ on the left side and a SSH chain with $K_1 > K_2$ on the right side. The periods of both chains in one supercell unit are 20. (b) Dependence of the interface states (red lines) on K_1/K_2 for the right SSH chain, while the left SSH chain ($K_1 < K_2$) remains unchanged. For simplicity, $K_1 + K_2$ is held constant in the calculations. The gray-shaded regions in both (a) and (b) denote the projection bulk bands.

than 0.08. According to the spring-mass model analysis, gaps I and III can be identified as the band-folding-induced gaps, while gap II is the original local resonant band gap. The pressure-field distribution of the eigenstate in one unit cell at the band edges of all three gaps is plotted in Fig. 3(c). For the left lattice, in gaps I and III, the lower band edges, viz., S1 and S5, are even modes since their field distributions are symmetric with respect to the central plane of the unit cell. Meanwhile, the upper band edges, viz., S2 and S6, are odd modes since their field distributions are antisymmetric with respect to the central plane of the unit cell. However, these symmetry properties are exactly reversed for the right lattice.

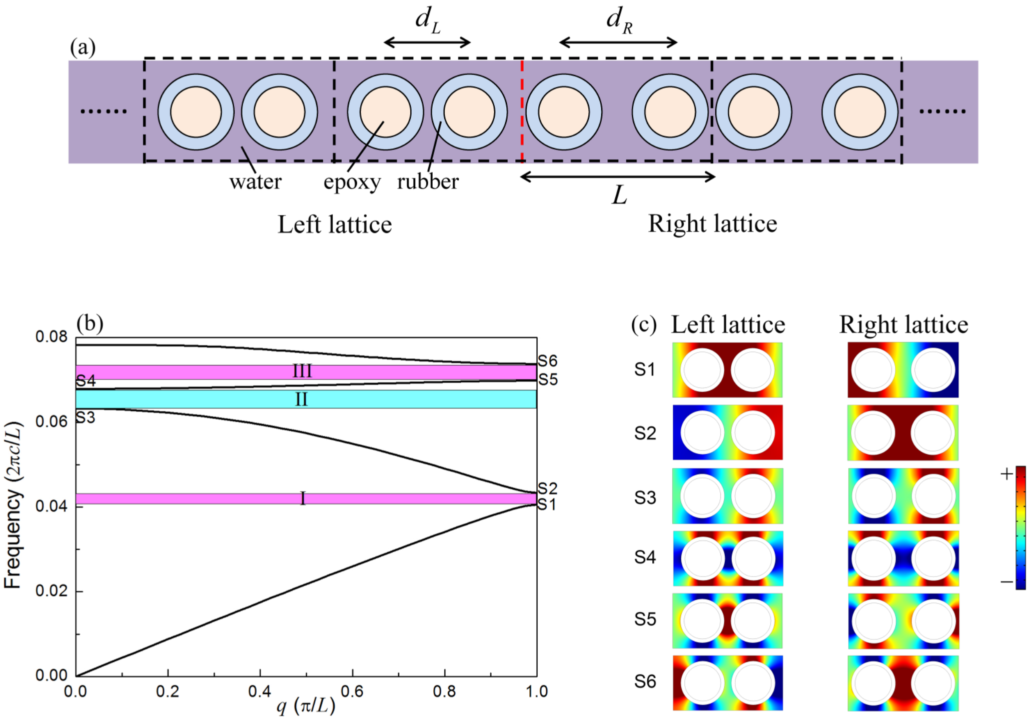

FIG. 3. (a) Configuration of a practical structural model of the connected SSH chain with local resonant unit cells. Each scatterer is a cylinder with an epoxy core wrapped in soft rubber, and all cylinders are immersed in water. The dashed black frames denote the unit cell. The separation between two individual cylinders in a unit cell is d_L for the left lattice and d_R for the right lattice. L is the lattice constant. The inner and outer radii of the cylinders are $0.165L$ and $0.2L$. The red dashed line denotes the interface between the two lattices. (b) Band structure of the left or right lattice. The frequencies are in units of $2\pi c/L$, where c is the acoustic wave velocity in water. All of the symbols have the same meanings as in Fig. 1(f). (c) Pressure-field distributions of band edges for the left and right lattices, where only the pressure fields in the water are shown.

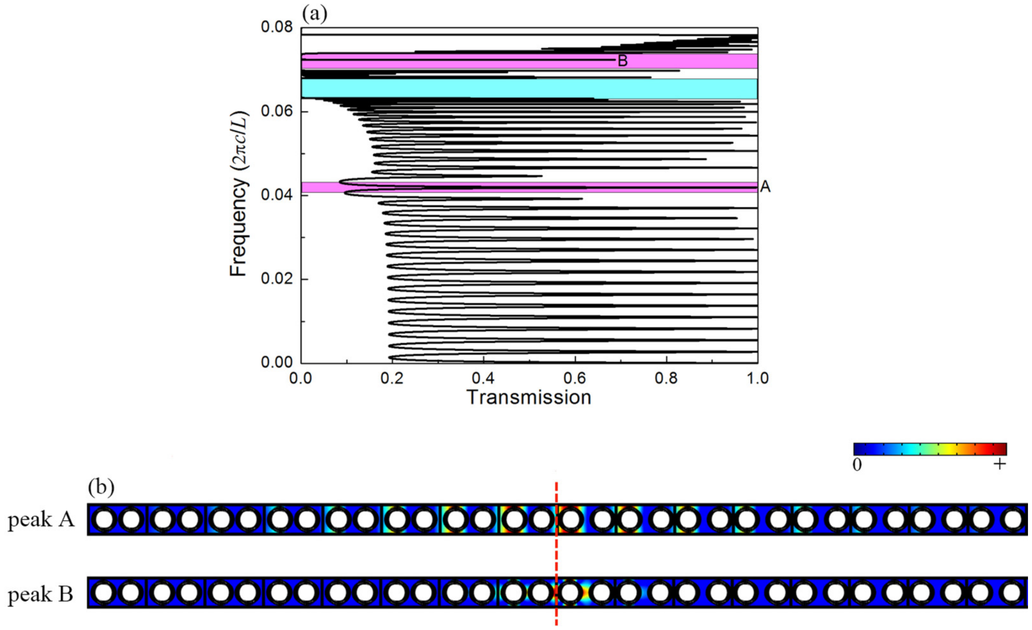

FIG. 4. (a) Transmission spectrum of a finite-size lattice shown in Fig. 3(a), where both the left and right lattices have eight periods. A and B denote the transmission peaks in the band gaps. (b) Absolute values of the pressure-field distributions (only in the background) of peaks A and B.

Thus, band inversion occurs in gaps I and III. However, for gap II of both the left and right lattices, the state at the lower band edge S3 is an even mode, while that at the upper band edge S4 is an odd mode. There is no band inversion in gap II.

Next we calculate the transmission spectrum of a finite-size lattice to examine the existence of topological interface states. The sample is composed of an eight-period left lattice with $d_L(<L/2)$ connected with an eight-period right lattice with $d_R(>L/2)$. From the transmission spectrum plotted in Fig. 4(a), two topological interface states, appearing as two sharp transmission peaks marked A and B, emerge in gaps I and III, respectively, while no transmission peak exists in gap II. The pressure-field distributions of these two peaks are plotted in Fig. 4(b). Both of them exhibit the typical field-distribution pattern of interface states: the field intensity is the strongest on the interface and rapidly decays away from the surface.

IV. CONCLUSION AND DISCUSSION

In this study, we apply the spring-mass model to demonstrate the band evolution and topological properties of 1D acoustic SSH chain systems with local resonant unit cells. Owing to band folding, two Bragg-like gaps can be produced in the subwavelength region. According to the Zak-phase calculations and band-inversion analysis, the topological interface states can only exist in the band-folding-induced gaps, and never in the original local resonant band gap. We further propose a practical structure that can yield topological interface states in the subwavelength region. Physically, the local resonant band gap is due to the singularity of effective mass of oscillators. When the frequency ω approaches the resonant frequency ω_0, the effective mass tends to infinity and the oscillators have no response to incident acoustic wave. In other words, near the resonant frequency, the band gap will definitely be opened. The lower and upper bands of local resonant band gap cannot meet each other to become a topological phase-transition point. Thus the essential condition to produce the "open-close-reopen," viz., band-inversion process, is absent. Obviously, the original local resonant band gap cannot support any topological interface states. However, that does not mean the topological interface states cannot be obtained in the subwavelength region. As shown in this paper, we can firstly produce pass bands in the subwavelength frequency region, and then the band-folding mechanism is utilized to open new gaps. Essentially these gaps are created by the different interactions between an oscillator and the oscillators neighboring it to the left and right. In practice, it is easy to achieve band inversion by adjusting the separation of two oscillators in a unit cell of a SSH chain and finally to obtain subwavelength topological interface states in a connected SSH chain system. We note that our spring-mass model can be described as a nearest-neighbor tight-binding model as each oscillator only interacts with its nearest-neighbor oscillators. However, for a general system with a more complex form of interaction (say for example, long-range hopping), the local resonant gap may get mixed with other band gaps. The topological property of the local resonant gap in that case will be considered and discussed in future works. In fact, a similar band-folding mechanism has been applied in the Bragg gaps in two-dimensional systems by other authors [17,30]. The technique proposed in this paper can be treated as a general method of obtaining topological edge states in the subwavelength region. It can be readily expanded to negative effective modulus systems, such as Helmholtz resonator chains [31], as well as two- and three-dimensional optical, mechanical, acoustic, and elastic systems.

ACKNOWLEDGMENTS

We thank Zhaoqing Zhang, Kun Ding, Anan Fang, Shubo Wang, Yixin Xiao, and Wenjie Chen for the helpful discussions. This work is supported by Research Grants Council, University Grants Committee, Hong Kong (Grant No. AoE/P-02/12).

APPENDIX A: EIGENVALUE EQUATION

For the monatomic chain schematically depicted in Fig. 1(a), the equations of motion for the nth unit cell are

$$M\frac{d^2u_n}{dt^2} = K(u_{n-1} + u_{n+1} - 2u_n) + 2G(v_n - u_n), \tag{A1}$$

$$m\frac{d^2v_n}{dt^2} = 2G(u_n - v_n), \tag{A2}$$

where u_n and v_n denote the displacements of masses M and m with respect to their equilibrium positions in the unit cell, respectively. The displacement of an infinite atomic chain has harmonic solution $u(v) = A_{u(v)}e^{i(kx-\omega t)}$, where A, k, and ω are the amplitude, wave number, and angular frequency, respectively. By substituting the harmonic solution, Eq. (A2) becomes

$$v_n = \frac{2G}{2G - m\omega^2}u_n. \tag{A3}$$

Substituting Eq. (A3) into Eq. (A1) to eliminate v_n, we obtain

$$-M_{\text{eff}}\omega^2u_n = K(u_{n-1} + u_{n+1} - 2u_n), \tag{A4}$$

where

$$M_{\text{eff}} = M + \frac{m\omega_0^2}{\omega_0^2 - \omega^2}, \quad \omega_0^2 = \frac{2G}{m}. \tag{A5}$$

Equation (A4) is the standard vibration equation of a periodic monatomic chain, and Eqs. (A4) and (A5) indicate that a local resonant unit cell can be regarded as an effective single oscillator with an effective mass M_{eff} [32–34]. Applying Bloch's theorem $u_{n\pm1} = e^{\pm iqL}u_n$ (where q is the Bloch wave number and $L = a$ is the lattice constant) in Eq. (A4), the dispersion relation for a monatomic chain can be obtained:

$$M_{\text{eff}}\omega^2 = 4K\sin^2\frac{qL}{2}. \tag{A6}$$

For the diatomic chain schematically depicted in Fig. 1(c), the equations of motion become

$$-M_{\text{eff}}\omega^2u_i = K_1(u_j - u_i) + K_2(u_{j-1} - u_i), \tag{A7}$$

$$-M_{\text{eff}}\omega^2u_j = K_2(u_{i+1} - u_j) + K_1(u_i - u_j). \tag{A8}$$

Applying Bloch's theorem $u_{i+1} = e^{iqL}u_i$, $u_{j-1} = e^{-iqL}u_j$, the above equations can be written in matrix form as

$$\begin{pmatrix} 0 & K_1 + K_2e^{-iqL} \\ K_1 + K_2e^{iqL} & 0 \end{pmatrix}\begin{pmatrix} u_i \\ u_j \end{pmatrix} = (K_1 + K_2 - M_{\text{eff}}\omega^2)\begin{pmatrix} u_i \\ u_j \end{pmatrix}, \tag{A9}$$

which is the eigenvalue equation of a diatomic chain.

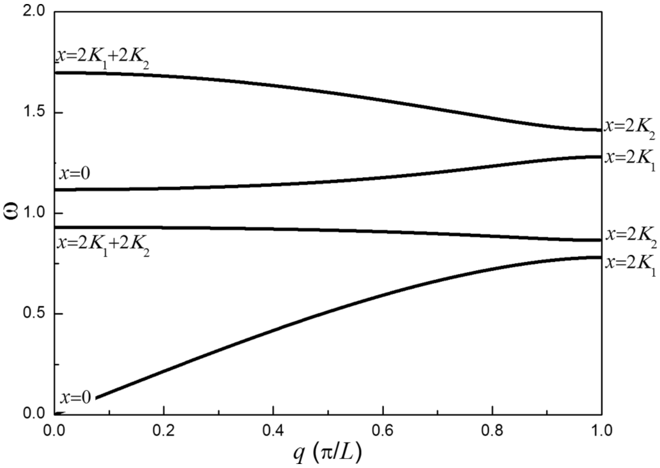

FIG. 5. Solutions of x in Eq. (B1) at all of the band edges.

APPENDIX B: DISPERSION RELATION SOLUTIONS AT THE BAND EDGES

Letting $x = M_{\text{eff}}\omega^2$ simplifies the dispersion relation in Eq. (3) in the main text to

$$\cos qL = 1 - \frac{x(2K_1 + 2K_2 - x)}{2K_1K_2}. \tag{B1}$$

For the pass bands, the Bloch wave number q should be real, yielding the inequality

$$\left|1 - \frac{x(2K_1 + 2K_2 - x)}{2K_1K_2}\right| \leqslant 1. \tag{B2}$$

Without loss of generality, it can be assumed that $K_1 < K_2$, making the solution of Eq. (B2)

$$0 \leqslant x \leqslant 2K_1 \quad \text{or} \quad 2K_2 \leqslant x \leqslant 2K_1 + 2K_2. \tag{B3}$$

At the band edges, i.e., $q = 0$ and $q = \pi/L$, the exact solutions of x can be obtained [using the equality sign in Eq. (B3)], which are marked in Fig. 5. It clearly reveals that the first and third band gaps are opened because $K_1 \neq K_2$. In addition, the second band gap is opened due to the singularity of M_{eff}, since $\omega_0 = 1.0$ is its central frequency. When $K_1 = K_2 = K$, x has a double root $2K$ at $q = \pi/L$, which corresponds to the band-crossing points.

APPENDIX C: SIGNS OF EIGENVECTORS AT THE BAND EDGES

The eigenvalue of Eq. (2) in the main text can be written as

$$\lambda = K_1 + K_2 - M_{\text{eff}}\omega^2 = \pm|K_1 + K_2e^{-iqL}|. \tag{C1}$$

The sign of the eigenvector in Eq. (4) in the main text is equivalent to the sign of λ, which is determined by the sign of $K_1 + K_2 - M_{\text{eff}}\omega^2$. Setting

$$\lambda(\omega) = 2K_1 + 2K_2 - M_{\text{eff}}\omega^2 = 2K_1 + 2K_2 - \left(M + \frac{m\omega_0^2}{\omega_0^2 - \omega^2}\right)\omega^2, \tag{C2}$$

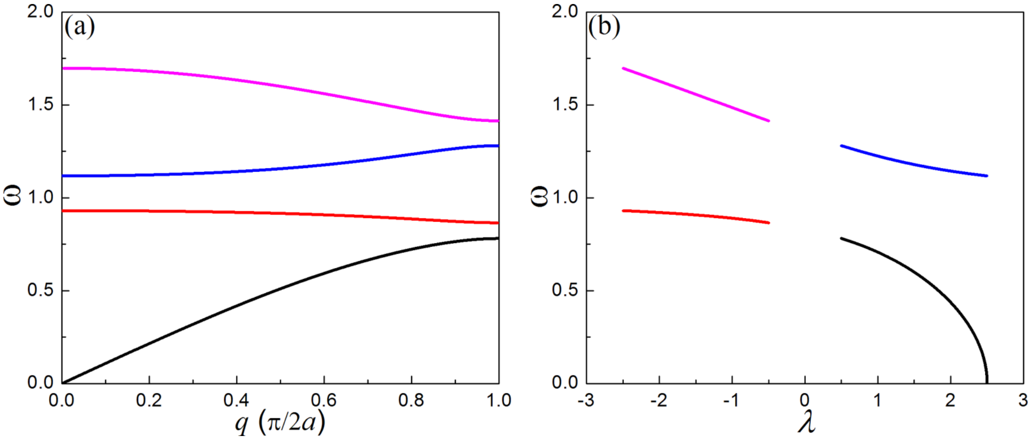

FIG. 6. (a) Band structure of SSH chain. All bands are distinguished by different colors. (b) Eigenvalues for all of the bands. The colors have one-to-one correspondence to those in (a).

then

$$\frac{d\lambda}{d\omega} = -2\omega M - \frac{2m\omega\omega_0^4}{(\omega_0^2-\omega^2)^2} < 0. \tag{C3}$$

Thus, $\lambda(\omega)$ is a monotonic decreasing function except at the jump at ω_0. Then, all of the four bulk bands in Fig. 1(f) in the main text can be divided into two sections: the first and second bulk bands are in the $\omega < \omega_0$ region, while the third and fourth bulk bands are in the $\omega > \omega_0$ region. Since $\lambda(\omega)$ is a decreasing function, in each section the lower (first and third) bands have positive eigenvalues and the upper (second and fourth) bands have negative eigenvalues, as clearly shown in Fig. 6. Then the signs of the eigenstates at all of the band edges can be calculated for $K_1 < K_2$ and $K_1 > K_2$. For example, when $K_1 < K_2$, at state S1 [marked in Fig. 1(c) in the main text],

$$\phi(q) = \arg(K_1 + K_2e^{-iqL})|_{qL=\pi} = \pi. \tag{C4}$$

Substituting Eq. (C4) into Eq. (4) in the main text, and noticing that the signs before the first two eigenvector components are positive since $\lambda > 0$,

$$\begin{aligned}&\operatorname{sgn}(u_i, v_i, u_j, v_j)^T\\&= \operatorname{sgn}\left(e^{i\phi(q)}, \frac{\omega_0^2}{\omega_0^2-\omega^2}e^{i\phi(q)}, 1, \frac{\omega_0^2}{\omega_0^2-\omega^2}\right)^T\\&= (-,-,+,+)^T.\end{aligned} \tag{C5}$$

Meanwhile, at state S2, $\phi(q)$ still equals π since it located on the Brillouin-zone boundary as well. However, $\lambda < 0$ now, so the eigenvector signs become

$$\begin{aligned}&\operatorname{sgn}(u_i, v_i, u_j, v_j)^T\\&= \operatorname{sgn}\left(-e^{i\phi(q)}, -\frac{\omega_0^2}{\omega_0^2-\omega^2}e^{i\phi(q)}, 1, \frac{\omega_0^2}{\omega_0^2-\omega^2}\right)^T\\&= (+,+,+,+)^T.\end{aligned} \tag{C6}$$

When $K_1 > K_2$, at both states S1 and S2,

$$\phi(q) = \arg(K_1 + K_2e^{-iqL})\big|_{qL=\pi} = 0. \tag{C7}$$

The eigenvector signs at S1 are

$$\begin{aligned}&\operatorname{sgn}(u_i, v_i, u_j, v_j)^T\\&= \operatorname{sgn}\left(e^{i\phi(q)}, \frac{\omega_0^2}{\omega_0^2-\omega^2}e^{i\phi(q)}, 1, \frac{\omega_0^2}{\omega_0^2-\omega^2}\right)^T\\&= (+,+,+,+)^T,\end{aligned} \tag{C8}$$

and the eigenvector signs at S2 are

$$\begin{aligned}&\operatorname{sgn}(u_i, v_i, u_j, v_j)^T\\&= \operatorname{sgn}\left(-e^{i\phi(q)}, -\frac{\omega_0^2}{\omega_0^2-\omega^2}e^{i\phi(q)}, 1, \frac{\omega_0^2}{\omega_0^2-\omega^2}\right)^T\\&= (-,-,+,+)^T.\end{aligned} \tag{C9}$$

Equations (C5), (C6), (C8), and (C9) distinctly exhibit a band inversion. The signs of the eigenstates at all of the other band edges can be obtained similarly.

APPENDIX D: CALCULATION OF ZAK PHASE

Since our eigenvalue problem [Eq. (2) in the main text] is not written as Hamiltonian form, the eigenvector [Eq. (4) in the main text] cannot be directly used in calculating Zak phase. The eigenvector should be normalized by the energy, so that it will definitely correspond to a Hamiltonian, even though its exact expression is unknown. At first, the displacement is converted into velocity

$$\frac{d}{dt}(u_i, v_i, u_j, v_j)^T = \left(\pm i\omega e^{i\phi(q)}, \pm i\omega\frac{\omega_0^2}{\omega_0^2-\omega^2}e^{i\phi(q)}, -i\omega, -i\omega\frac{\omega_0^2}{\omega_0^2-\omega^2}\right)^T. \tag{D1}$$

It should be noted that ω is also a function of q. Normalize the eigenvector as

$$
\begin{aligned}
|\Psi\rangle &= \frac{1}{\sqrt{M + m\left(\frac{\omega_0^2}{\omega_0^2-\omega^2}\right)^2}}\left(\pm\sqrt{\frac{M}{2}}e^{i\phi(q)}, \pm\sqrt{\frac{m}{2}}\frac{\omega_0^2}{\omega_0^2-\omega^2}e^{i\phi(q)}, -\sqrt{\frac{M}{2}}, -\sqrt{\frac{m}{2}}\frac{\omega_0^2}{\omega_0^2-\omega^2}\right)^T \\
&= (\pm A(q)e^{i\phi(q)}, \pm B(q)e^{i\phi(q)}, A(q), B(q))^T, \qquad \text{(D2)}
\end{aligned}
$$

where $2(A^2 + B^2) = 1$. Then the inner product of the eigenvector with itself gives the kinetic energy. Substituting $|\Psi\rangle$ into Eq. (5) in the main text,

$$
\begin{aligned}
\theta &= i\int_{-\pi/L}^{\pi/L}\left[(\pm A(q)e^{i\phi(q)})^*\frac{\partial(\pm A(q)e^{i\phi(q)})}{\partial q} + (\pm B(q)e^{i\phi(q)})^*\frac{\partial(\pm B(q)e^{i\phi(q)})}{\partial q} + A(q)\frac{\partial A(q)}{\partial q} + B(q)\frac{\partial B(q)}{\partial q}\right]dq \\
&= i\int_{-\pi/L}^{\pi/L}\left[2A(q)\frac{\partial A(q)}{\partial q} + iA^2(q)\frac{\partial\phi(q)}{\partial q} + 2B(q)\frac{\partial B(q)}{\partial q} + iB^2(q)\frac{\partial\phi(q)}{\partial q}\right]dq \\
&= i\int_{-\pi/L}^{\pi/L}\left[\frac{\partial(A^2(q)+B^2(q))}{\partial q} + i(A^2(q)+B^2(q))\frac{\partial\phi(q)}{\partial q}\right]dq \\
&= -\frac{1}{2}\int_{-\pi/L}^{\pi/L}\frac{\partial\phi(q)}{\partial q}dq \\
&= -\frac{1}{2}\left[\phi\left(\frac{\pi}{L}\right) - \phi\left(-\frac{\pi}{L}\right)\right] \qquad \text{(D3)}
\end{aligned}
$$

[1] X. L. Qi and S. C. Zhang, Rev. Mod. Phys. **83**, 1057 (2011).

[2] M. Z. Hasan and C. L. Kane, Rev. Mod. Phys. **82**, 3045 (2010).

[3] R. Süsstrunk and S. D. Huber, Science **349**, 47 (2015).

[4] C. L. Kane and T. C. Lubensky, Nat. Phys. **10**, 39 (2014).

[5] J. Paulose, B. G. Chen, and V. Vitelli, Nat. Phys. **11**, 153 (2015).

[6] F. D. M. Haldane and S. Raghu, Phys. Rev. Lett. **100**, 013904 (2008).

[7] M. C. Rechtsman, J. M. Zeuner, Y. Plotnik, Y. Lumer, D. Podolsky, F. Dreisow, S. Nolte, M. Segev, and A. Szameit, Nature (London) **496**, 196 (2013).

[8] L. Lu, J. D. Joannopoulos, and M. Soljačić, Nat. Photon. **8**, 821 (2014).

[9] J. Lu, C. Qiu, L. Ye, X. Fan, M. Ke, F. Zhang, and Z. Liu, Nat. Phys. **13**, 369 (2017).

[10] M. Xiao, W.-J. Chen, W.-Y. He, and C. T. Chan, Nat. Phys. **11**, 920 (2015).

[11] Z. Yang, F. Gao, X. Shi, X. Lin, Z. Gao, Y. D. Chong, and B. Zhang, Phys. Rev. Lett. **114**, 114301 (2015).

[12] Y. Peng, C. Qin, D. Zhao, Y. Shen, X. Xu, M. Bao, H. Jia, and X. Zhu, Nat. Commun. **7**, 13368 (2016).

[13] P. Wang, L. Lu, and K. Bertoldi, Phys. Rev. Lett. **115**, 104302 (2015).

[14] A. B. Khanikaev, R. Fleury, S. H. Mousavi, and A. Alù, Nat. Commun. **6**, 8260 (2015).

[15] S. H. Mousavi, A. B. Khanikaev, and Z. Wang, Nat. Commun. **6**, 8682 (2015).

[16] Z.-G. Chen and Y. Wu, Phys. Rev. Appl. **5**, 054021 (2016).

[17] C. He, X. Ni, H. Ge, X. Sun, Y. Chen, M. Lu, X. Liu, and Y. Chen, Nat. Phys. **12**, 1124 (2016).

[18] J. Zak, Phys. Rev. Lett. **62**, 2747 (1989).

[19] M. Xiao, Z. Q. Zhang, and C. T. Chan, Phys. Rev. X **4**, 021017 (2014).

[20] M. Xiao, G. Ma, Z. Yang, P. Sheng, Z. Q. Zhang, and C. T. Chan, Nat. Phys. **11**, 240 (2015).

[21] W. P. Su, J. R. Schrieffer, and A. J. Heeger, Phys. Rev. Lett. **42**, 1698 (1979).

[22] E. J. Meier, F. A. An, and B. Gadway, Nat. Commun. **7**, 13986 (2016).

[23] C. W. Ling, M. Xiao, C. T. Chan, S. F. Yu, and K. H. Fung, Opt. Express **23**, 2021 (2015).

[24] H. Deng, X. Chan, N. C. Panoiu, and F. Ye, Opt. Lett. **41**, 4281 (2016).

[25] A. Blanco-Redondo, I. Andonegui, M. J. Collins, G. Harari, Y. Lumer, M. C. Rechtsman, B. J. Eggleton, and M. Segev, Phys. Rev. Lett. **116**, 163901 (2016).

[26] C. Poli, M. Bellec, U. Kuhl, F. Mortessagne, and H. Schomerus, Nat. Commun. **6**, 6710 (2015).

[27] Z. Yang, F. Gao, and B. Zhang, Sci. Rep. **6**, 29202 (2016).

[28] Z. Yang and B. Zhang, Phys. Rev. Lett. **117**, 224301 (2016).

[29] Z. Liu, X. Zhang, Y. Mao, Y. Y. Zhu, Z. Yang, C. T. Chan, and P. Sheng, Science **289**, 1734 (2000)

[30] Z. Zhang, Q. Wei, Y. Cheng, T. Zhang, D. Wu, and X. Liu, Phys. Rev. Lett. **118**, 084303 (2017).

[31] N. Fang, D. Xi, J. Xu, M. Ambati, W. Srituravanich, C. Sun, and X. Zhang, Nat. Mater. **5**, 452 (2006).

[32] H. H. Huang, C. T. Sun, and G. L. Huang, Int. J. Eng. Sci, **47**, 610 (2009).

[33] S. Yao, X. Zhou, and G. Hu, New J. Phys. **10**, 043020 (2008).

[34] H. H. Huang and C. T. Sun, New J. Phys. **11**, 013003 (2009).